

Modulating product selectivity in lignin electroreduction with a robust metallic glass catalyst

Received: 1 November 2024

Accepted: 26 March 2025

Published online: 10 April 2025



Ziqi Zhai^{1,2,5}, Yumiao Lu^{1,2,5}, Lufei Ouyang³, Junfeng Lu^{1,2}, Wei-Lu Ding^{1,2}, Bobo Cao¹, Yanlei Wang¹, Feng Huo⁴, Qiu Zhao¹, Weihua Wang³✉, Suojiang Zhang¹✉ & Hongyan He^{1,2,4}✉

Converting the lignin into value-added chemicals and fuels represents a promising way to upgrade lignin. Here, we present an effective electrocatalytic approach that simultaneously modulates the depolymerization and hydrogenation pathways of lignin model compounds within a single reaction system. By fine-tuning the pH of the electrolyte, we achieve a remarkable shift in product selectivity, from acetophenone (with selectivity >99%) to 1-phenylethanol (with selectivity >99%), while effectively preventing over-hydrogenation. The robust metallic glass (MG) catalyst, endowed with an amorphous structure, demonstrates high stability, activity, and full recyclability across over 100 consecutive cycles in ionic liquid electrolytes. The relatively strong affinity of the MG catalyst for the substrate during the initial reaction stage, in conjunction with its weaker binding to the phenolic product, as the reaction progresses, creates a delicate balance that optimizes substrate adsorption and product desorption, which is pivotal in driving the cascade hydrogenation process of acetophenone. This work opens versatile pathways for lignin upgrading through integrated tandem reactions and expands the scope of catalyst design with amorphous structures.

The production of commodity chemicals and fuels relies heavily on the petrochemical industry, which has precipitated severe environmental issues, raised health concerns, and threatened biodiversity¹. Lignin, the most abundant renewable source of aromatics on our planet, presents itself as a compelling alternative feedstock to petroleum². Efficient conversion of lignin into monocyclic hydrocarbons is pivotal and highly desirable for the sustainability of biorefineries^{3,4} (Fig. 1a). However, the complex, branched, three-dimensional amorphous structure of lignin, composed of phenylpropane units linked by diverse C-C and C-O bonds, imparts it with considerable chemical and physical resilience, yet challenges its efficient conversion into high-value

chemicals^{5,6}. The request for effective lignin depolymerization and upgrading strategies is gaining increasing attention.

Traditional chemical and pyrolysis techniques can break most inter-unit bonds within lignin but suffer from solvent and energy consumption. In particular, the complicated side reactions that accompany the sustained heating process generate an array of by-products, diverting from the target monomer^{7–9} (Fig. 1b). Recently, electrocatalysis has emerged as a promising strategy for the conversion of lignin to low molecular weight chemicals¹⁰. This approach leverages electrical energy to activate lignin molecules on the catalyst surface under mild conditions, offering substantial economic

¹Beijing Key Laboratory of Solid State Battery and Energy Storage Process, State Key Laboratory of Mesoscience and Engineering, CAS Key Laboratory of Green Process and Engineering, Institute of Process Engineering, Chinese Academy of Sciences, Beijing 100190, China. ²School of Chemical Engineering, University of Chinese Academy of Sciences, Beijing 100190, China. ³Institute of Physics, Chinese Academy of Sciences, Beijing 100190, China. ⁴Longzihu New Energy Laboratory, Zhengzhou Institute of Emerging Industrial Technology, Zhengzhou 450000, China. ⁵These authors contributed equally: Ziqi Zhai, Yumiao Lu. ✉e-mail: whw@iphy.ac.cn; sjzhang@ipe.ac.cn; hyhe@ipe.ac.cn

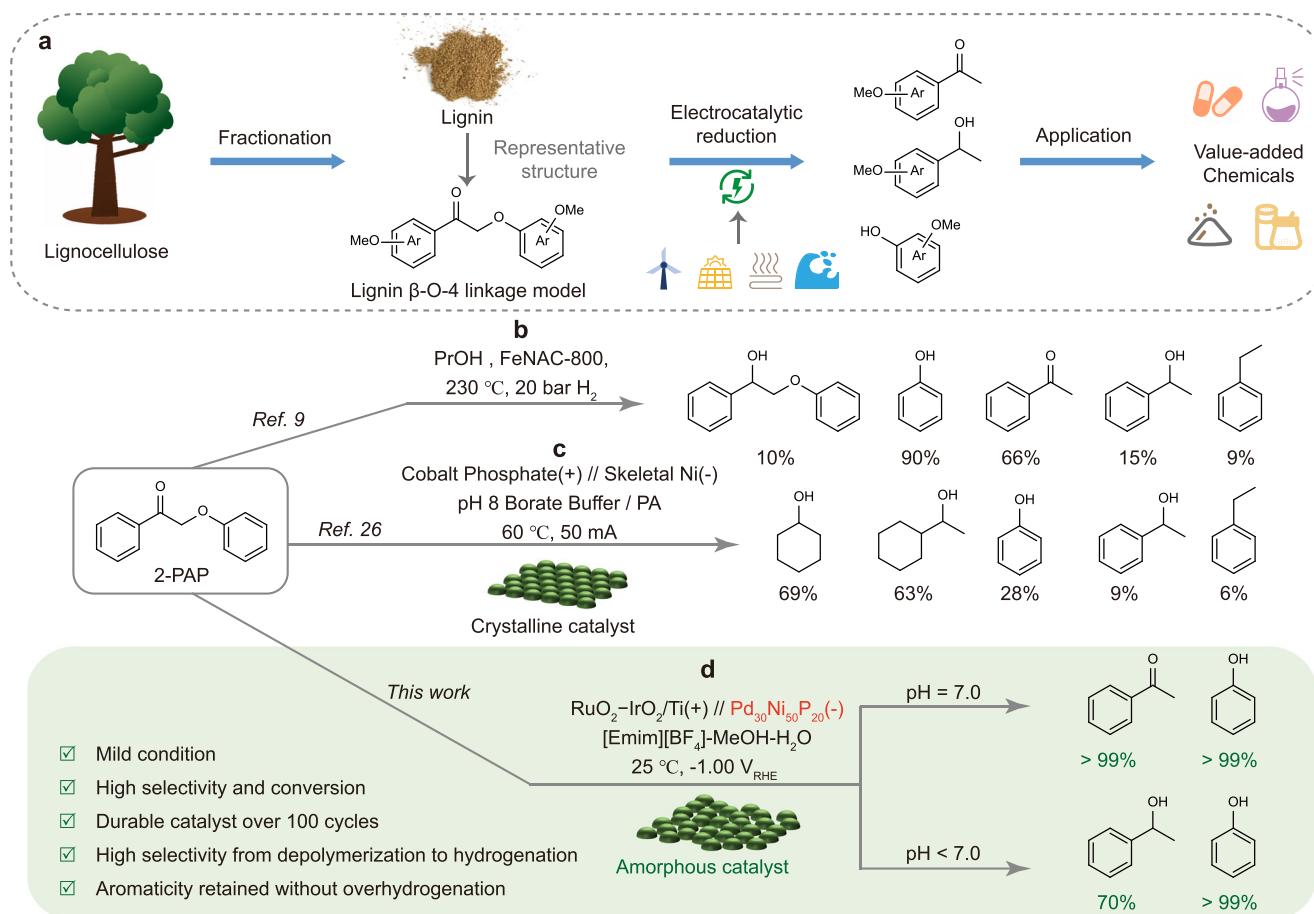


Fig. 1 | Degradation strategies for the high-value utilization of lignin. a Valorization strategy of lignin. **b** Hydrogenolysis and **c** electrocatalytic cleavage of the β -O-4 bond in lignin model compound 2-phenoxyacetophenone (2-PAP). **d** Proposed electroreduction and hydrogenation of 2-PAP by a metallic glass catalyst.

potential¹¹. Often, the focus has been directed towards the oxidative depolymerization of lignin to aromatics bearing aldehydes and carboxylic acids, whereas reductive pathways remain underexplored¹². In fact, the aromatics derived from electroreduction also possess attractive properties for applications in bio-oils and biological funneling to value-added chemicals, complementing the product spectrum obtained from oxidative methods^{13–16}. Despite this, lignin electroreduction is still in its infancy, with a primary obstacle being the development of potent and economically viable electrocatalysts^{17,18}.

To achieve complete depolymerization, electroreductive systems often incorporate noble metal catalysts, such as Pd, Pt, Ru, Rh, or Ir^{19–22}, known for their remarkable catalytic activity. However, economically, single-atoms and nanoparticles are more desirable choices than their bulk noble metal counterparts^{22–24}. However, the small size of these catalysts often leads to instability, which compromises their operational lifespan in practical scenarios. For example, Wang et al. reported an impressive yield of phenolic monomers (41 wt%) with atomically dispersed Pd/ZnO/C catalysts for birch wood degradation, yet the yield decreased to 32 wt% after just three cycles, highlighting the catalyst's limited stability²⁵. Beyond instability, noble metals, with their propensity for hydrogenation, can induce over-hydrogenation during electroreduction, which is undesirable. For instance, Garedew et al. utilized a ruthenium catalyst supported on the activated carbon cloth to degrade lignin dimers electrocatalytically. Although the process is efficient, the aromaticity of the final products is compromised, and cyclohexanol is formed instead²⁰. Therefore, the valorization of lignin requires both effective degradation and selective hydrogenation, yet this field currently lacks efficient electrocatalysts capable of selectively producing aromatic products²⁶ (Fig. 1c).

To surmount these hurdles, researchers have turned their attention to the structural design of catalysts. A significant revelation is that amorphous structures can markedly bolster catalytic performance²⁷. For instance, Baghestani et al. explored how structural disorder can alter the intrinsic thermodynamic stability of catalysts, suggesting the advantage of amorphous structure for proton and electron transfer during molecular activation²⁸. Metallic glass (MG), as a quintessential amorphous material, has shown promise in applications such as the hydrogen evolution reaction (HER), oxygen reduction reaction (ORR), fuel cells, and capacitive sensors^{29–31}. Building on these insights, we hypothesize that MG could offer a highly effective platform for lignin electroreduction, potentially unlocking high-value utilization of biomass resources.

In addition to catalyst selection, the electrolyte plays a crucial role in modulating the electrocatalytic conversion of lignin. There is a burgeoning interest in organic solvents like ionic liquids (ILs) and deep eutectic solvents (DESS)^{32–35} as alternatives to traditional alkaline solutions. These solvents offer several advantages, including lower volatility, improved lignin solubility, a wider electrochemical window, and stronger interactions between lignin and catalysts^{36,37}. Preliminary studies have already demonstrated the unique benefits of IL electrolytes in lignin degradation^{38–41}, with Liu et al. successfully achieving targeted cleavage of C-O/C-C bonds in lignin via electrocatalytic conversion in ILs^{38,41}. However, effective screening of ILs, given the vast array of cations and anions, and understanding their solvent effects, which are often used to dilute ILs for conductivity enhancement, remain a formidable challenge that demands further investigation.

In this study, we present an effective electrocatalytic system, integrating MG catalysts and IL electrolyte, designed to enable complete depolymerization of lignin model compounds followed by

selective hydrogenation under ambient conditions (Supplementary Fig. 1 and Fig. 1d). A key feature of the hydrogenation process is its ability to preserve the aromaticity of the resulting products. Through a systematic selection of typical ILs based on their electrochemical windows, and extensive studies into the effects of organic solvents, such as methanol (MeOH) and acetonitrile (MeCN), as well as water, we developed a [Emim][BF₄]-MeOH-H₂O ternary electrolyte system that optimizes the catalytic performance. The synthesized MG ribbon, serving as both electrode and catalyst, exhibits superior stability, reactivity, and recyclability across over 100 consecutive electrocatalytic cycles. The system ensures complete substrate conversion, achieving product yields exceeding 99% with hydrogenation product selectivity above 99%. Moreover, the designed electrocatalytic system performs well on oxidized birch lignin, yielding vanillic acid as the primary product. This approach not only opens a promising avenue for lignin valorization but also contributes to the broader goal of sustainable chemistry by harnessing renewable resources and advancing efficient catalytic processes.

Results

Characterization of the Pd-Ni-P MG catalyst

Pd and Ni metals are widely recognized as promising electrode materials for electroreduction reactions, serving as catalytically active sites for lignin depolymerization and hydrogenation during cathodic processes. In addition, doping non-metallic elements, such as P and B, has shown to be effective in modulating the electronic structure of PdNi alloys, potentially boosting their electroreductive performance^{42,43}. Based on these findings, we synthesized a series of Pd-Ni-P MG cathodes to investigate their potential for lignin electroreduction. As illustrated in Fig. 2a, the synthesized MG ribbons with a thickness of approximately 15 μm , significantly reduce the usage of the noble metal Pd while providing superior elasticity compared to brittle crystalline materials. This flexibility enables the MG ribbons to conformally wrap around various solid surfaces, allowing for tunable electrode surface areas (Supplementary

Fig. 2). Electrical conductivity measurements confirm that these MG ribbons exhibit high conductivity, making them suitable for use as electrode materials (Supplementary Fig. 3). Notably, the same MG electrode was employed consistently throughout all experiments, and a series of characterizations, including X-ray diffraction (XRD), differential scanning calorimetry (DSC), X-ray photoelectron spectroscopy (XPS), scanning electron microscopy (SEM), high-resolution transmission electron microscopy (HRTEM), and Fast Fourier Transform (FFT), were conducted to verify the stability and activity of the amorphous structure even after 100 consecutive electrocatalytic cycles (Supplementary Figs. 4–9 and Supplementary Table 8). This durability underscores the robust stability of the MG ribbon in electroreduction and highlights its potential for facile recycling.

In this study, three different compositions of MG ribbons, Pd₃₀Ni₅₀P₂₀, Pd₄₀Ni₄₀P₂₀, and Pd₅₀Ni₃₀P₂₀ (in atomic percentage), were synthesized, in which the molar fraction of P was held constant while varying the Pd/Ni molar ratio. Energy dispersive X-ray (EDX) mapping reveals a uniform distribution of Pd, Ni, and P within the MG ribbons, confirming the successful doping of P into PdNi matrix and matching the expected atomic mass ratios (Supplementary Fig. 4). XRD characterizations confirm the amorphous nature of the materials, with broad diffraction peaks observed in the range of 35–45° (Fig. 2b) and demonstrating the successful preparation of a long-range disordered structure. SAXS-WAXS measurements further support the amorphous nature, showing no sharp diffraction peaks (Supplementary Fig. 5b). HRTEM and FFT analyses were also performed to corroborate these findings. The HRTEM images display a labyrinthine pattern, and the FFT analysis exhibits a broad scattering halo without distinct crystalline diffraction spots, thereby confirming the amorphous characteristics of the MG ribbons (Fig. 2c).

The thermodynamic data obtained from DSC (Supplementary Fig. 6a) reveal obvious glass transition (T_g) and crystallization (T_x) temperatures. The high T_x values observed for these ribbons, below which the amorphous structure remains stable, suggest their potential

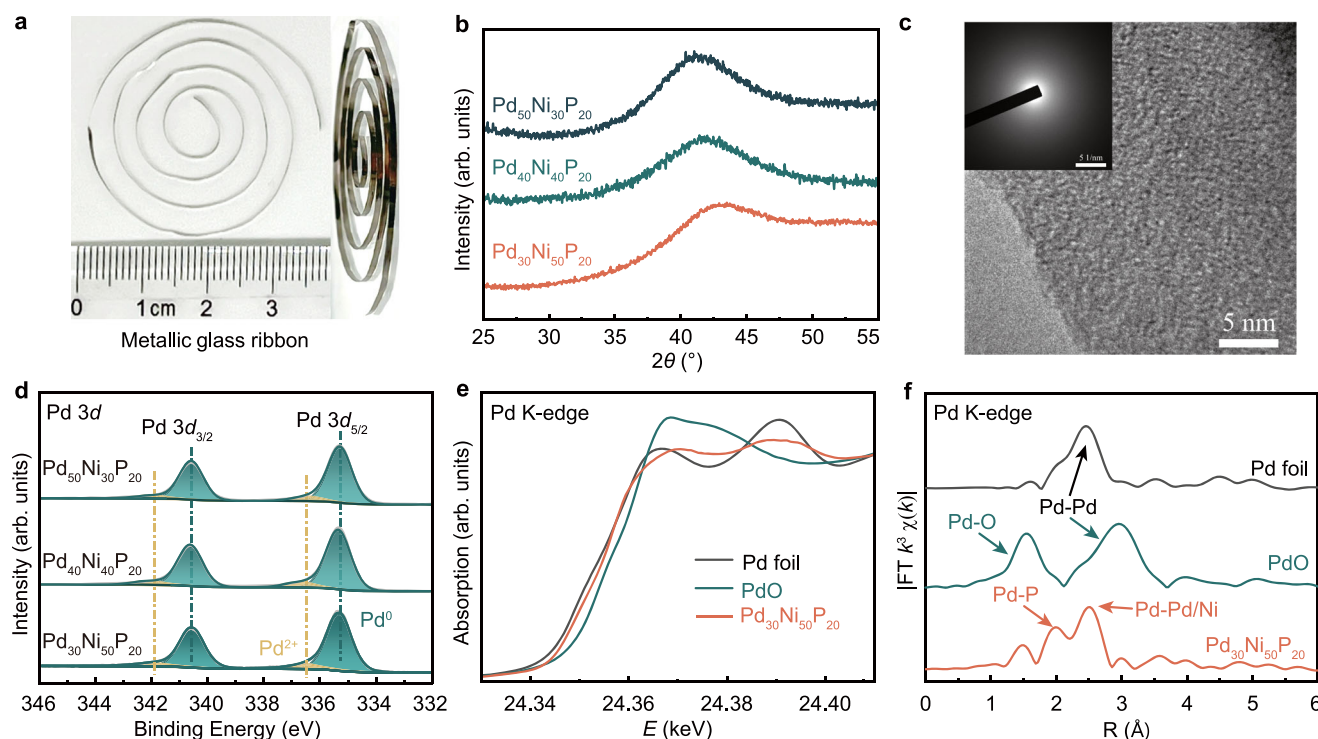


Fig. 2 | Structural characterization of MG ribbons. **a** Macroscopic view and **b** XRD spectra of different MG ribbons. **c** HRTEM image and the correlated FFT pattern (inset) of the Pd₃₀Ni₅₀P₂₀ MG ribbon. **d** High-resolution XPS spectra of Pd 3d for

different MG ribbons. **e** Pd K-edge XANES spectra and **f** EXAFS Fourier transformed k^2 -weighted $\chi(k)$ -function for Pd K-edge. Source data for Fig. 2b, d, f are provided as a Source Data file.

applicability in high-temperature electrochemical environments. Notably, both T_g and T_x values increase with a decreasing Pd/Ni molar ratio, indicating enhanced thermal stability. The surface valence states of the elements, as well as the electron transfer between Pd, Ni and P, were determined by XPS (Fig. 2d and Supplementary Fig. 10). Fine deconvolution of Pd 3d and Ni 2p peaks reveals binding energies corresponding to Pd⁰, Pd²⁺ and Ni⁰, Ni²⁺ species, indicating the coexistence of metallic and oxidized states of metal elements. Among the three MG ribbons, the predominant metallic states of Pd and Ni contribute to a strong reducing ability of the catalysts. The fitting results indicate that the Pd species in Pd₃₀Ni₅₀P₂₀ exhibit lower binding energies compared to those in MGs with higher Pd content, while the Ni and P species display higher binding energies, indicating electron transfer from Pd to Ni and P with increasing Pd content, potentially diminishing the reducing ability of Pd. After electroreduction, an overall increase in binding energies for Pd and Ni species is observed in the Pd₃₀Ni₅₀P₂₀ MG (Supplementary Fig. 8), and the Pd⁰/Pd²⁺ ratio decreases from 6.86 to 6.52, further confirming the catalytic activity of Pd and Ni during the reduction process. X-ray absorption fine structure (XAFS) spectrum was conducted to investigate the local electronic structure and atomic arrangement of Pd in the Pd₃₀Ni₅₀P₂₀ MG. The normalized X-ray absorption near edge structure (XANES) spectrum (Fig. 2e) shows that the Pd K-edge absorption energy in Pd₃₀Ni₅₀P₂₀ lies between that of Pd foil and PdO₂, indicating a positive charge on the Pd element, consistent with the XPS results. The Fourier-transformed extended X-ray absorption fine structure (EXAFS) spectrum of the Pd₃₀Ni₅₀P₂₀ exhibits two prominent peaks resonating at 1.98 Å and 2.51 Å (Fig. 2f), corresponding to Pd-P and Pd-Pd/Ni scattering, respectively⁴⁴. These results further support the interaction between Pd and Ni atoms in the Pd₃₀Ni₅₀P₂₀ catalyst.

Electrocatalytic system

The selection of catalysts with high catalytic activity and stable electrolytes is crucial for lignin electroreduction. ILs, known for their wide

electrochemical windows, high thermal stability, high conductivity, and good solubility of lignin, have emerged as promising alternatives to traditional alkaline electrolytes. In this study, eight ILs with straightforward synthesis processes and wide electrochemical windows were selected: [Emim][BF₄], [Bmmim][BF₄], [Emmim][BF₄], [Py₁₄][BF₄], [N₄₄₄₁][BF₄], [Emim][NTf₂], [Py₁₄][NTf₂] and [N₃₁₁₁][NTf₂] (Supplementary Fig. 11). To mitigate the high viscosity of these ILs, an equal volume of MeCN was added to each IL. Cyclic voltammetry (CV) tests were then conducted to evaluate the electrochemical behavior of these eight electrolyte systems using 2-phenoxyacetophenone (2-PAP) as the substrate (Supplementary Figs. 12a, b). As shown in Fig. 3a, two obvious reduction peaks are observed at -0.98 V_{RHE} (E_{p1}) and -1.24 V_{RHE} (E_{p2}), which, according to the literature, correspond to the electron transfer processes from the catalyst to the substrate and from the catalyst to the acetophenone product resulting from substrate depolymerization⁴⁵. Theoretically, a lower voltage indicates a reduced energy barrier and lower energy consumption in electroreduction, which is favorable for superior performance. Among the evaluated ILs, the [Emim][BF₄] exhibits the lowest peak potential, making it the optimal electrolyte for subsequent experiments (Fig. 3b).

To further assess the catalytic performance of the MG ribbons, similar CV tests were performed using the MG ribbons as the working electrode and [Emim][BF₄]-MeCN as the electrolyte (Supplementary Figs. 12c, d). The presence of the two reduction peaks further confirms the electroreductive capacity of the MG catalysts. As depicted in Fig. 3c, the peak currents (i_{p1} and i_{p2}) increase significantly with decreased Pd content, implying enhanced electron transfer between the catalysts and the substrates. Furthermore, among the three MG catalysts, the Pd₃₀Ni₅₀P₂₀ exhibits a higher overpotential for hydrogen evolution reaction (HER) and a lower charge transfer resistance in electrochemical impedance spectroscopy (EIS) (Supplementary Fig. 13). These results indicate that Pd₃₀Ni₅₀P₂₀ MG facilitates more efficient electron transfer and effectively suppresses HER during the electroreduction process, which is conducive to effective lignin

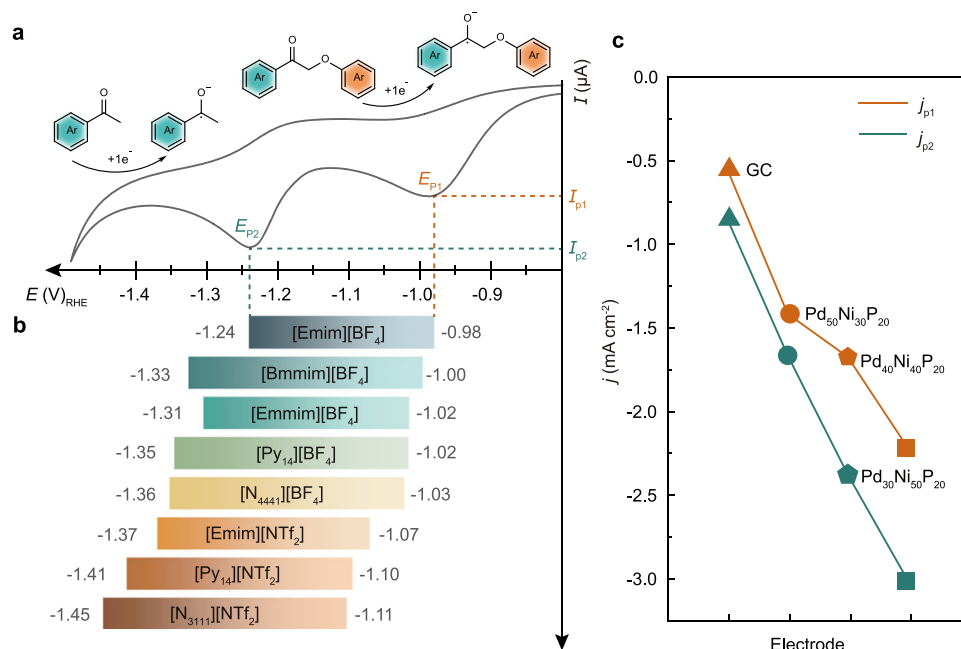


Fig. 3 | Construction of the electrocatalytic system for the lignin model compound of 2-PAP. a Cyclic voltammetry (CV) curve of 2-PAP in the [Emim][BF₄] electrolyte with glassy carbon (GC) as the electrode. **b** The peak potentials of two reduction peaks in eight different ILs. The reaction processes corresponding to the two peaks are illustrated. **c** The peak currents of the two reduction peaks for 2-PAP in the [Emim][BF₄] electrolyte are shown for different MG ribbons. Reaction

conditions: H-cell, ILs-MeCN (1:1, v/v), 5 mM 2-PAP, scan rate of 0.05 V s⁻¹, a three-electrode system with (a, b) a glassy carbon (GC) electrode or (c) MG ribbons as the working electrode, a Pt wire counter electrode, and an Ag/AgCl reference electrode. The potential values are not iR-corrected. Source data for Fig. 3 are provided as a Source Data file.

depolymerization. Therefore, the Pd₃₀Ni₅₀P₂₀ catalyst, in conjunction with the [Emim][BF₄] electrolyte, was selected to form an electrocatalytic system to further explore the electroreduction of lignin model compounds.

Lignin electroreduction

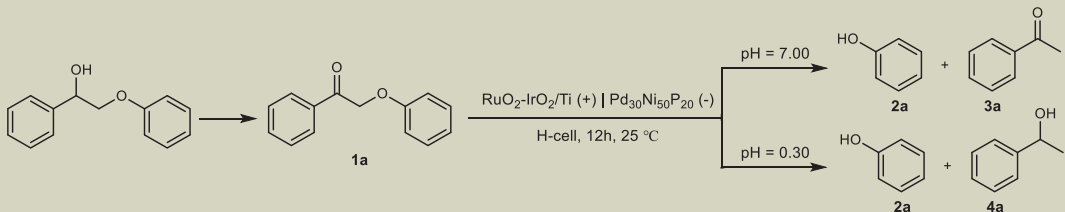
Effective cleavage of the C-O bond in β-O-4 model compounds has been the focus of prior studies, which typically employ a stepwise strategy: first, oxidation of the C_α-OH to C_α=O, and then performing electrolysis, which effectively lowers the dissociation energy of the C-O bond by 40–50 kJ mol⁻¹, as reported in the literature^{46–48}. Based on this, we adopted a similar two-step electroreduction approach, as outlined in Table 1. Initially, the lignin model compound was chemically oxidized, followed by depolymerization through electroreduction under a constant potential. To our delight, the Pd₃₀Ni₅₀P₂₀-[Emim][BF₄] electrocatalytic system exhibits higher conversions of 2-PAP across different electrolytes. In particular, for the binary electrolytes [Emim][BF₄]-MeCN, [Emim][BF₄]-MeOH, and [Emim][BF₄]-H₂O, the volume ratio was optimized to maximize the conductivity of the electrolyte (Supplementary Fig. 14a).

As reported in previous work, [Emim][BF₄]-MeCN has shown promising performance for lignin electroreduction³⁸. Here, a high conversion of 97% is achieved in the [Emim][BF₄]-MeCN electrolyte (Table 1, entry 1). The reduction voltage was selected based on the CV curve (Supplementary Fig. 14b). Density functional theory (DFT) calculations revealed that the interaction energy between two 2-PAP molecules is significantly favorable at -0.428 eV (Fig. 4a and

Supplementary Fig. 14c), indicating improved solubility of lignin model compounds in this electrolyte. However, the acetophenone (**3a**) yield is only 27%, probably due to the relatively slow proton transfer ability of MeCN, which further leads to the dimerization of the **3a** intermediate during continuous electroreduction⁴⁵. In contrast, the use of nucleophilic reagent MeOH can increase the **3a** yield to 65% due to its superior proton transfer capabilities, although the conversion decreases to 86% (Table 1, entry 2). The more negative interaction energy of lignin molecules in MeOH (-0.906 eV) results in weaker substrate adsorption on the electrode, thus hindering the overall conversion. To further optimize the process, we incorporated H₂O into the electrolyte system, leveraging its superior proton transfer potential. The [Emim][BF₄]-H₂O electrolyte increases the degradation efficiency, achieving a conversion of 98%, with yields of 82% for **3a** and 87% for phenol (**2a**) (Table 1, entry 3). When water was added at half the volume of the IL (Supplementary Fig. 14d), the degradation performance was optimal, with a conversion of 98% and yields of 96% for **2a** and 94% for **3a**.

However, the addition of water is found to negatively affect the solubility of other substrates with increased methoxy groups, thereby reducing the conversion rates (Supplementary Fig. 15a). To overcome this, MeOH was reincorporated into the [Emim][BF₄]-H₂O system, creating a ternary electrolyte, [Emim][BF₄]-MeOH-H₂O, with a volume ratio of 1:1:1. In this ternary electrolyte, the IL has the dual function of both solubilizing lignin and enhancing electrical conductivity (Table 1, entries 16–17)⁴⁹. MeOH contributes by enhancing lignin dissolution and facilitating proton transfer (Supplementary Fig. 15a, b), while water

Table 1 | Optimization of reaction conditions for the lignin model compound of 2-PAP



No.	E (V) _{RHE} ⁱ	Catholyte	Anolyte pH ⁱⁱ	Conv. (%) ⁱⁱⁱ	Product yield (%) ⁱⁱⁱ		
					2a	3a	4a
1	-1.15	IL-MeCN	7.00	97	79	27	-
2	-1.00	IL-MeOH	7.00	86	60	65	-
3	-1.00	IL-H ₂ O	7.00	98	87	82	-
4	-1.00	IL-MeOH- H ₂ O	7.00	>99	>99	>99	-
5	-0.80	IL-MeOH- H ₂ O	7.00	36	23	13	-
6	-0.90	IL-MeOH- H ₂ O	7.00	73	74	61	-
7	-1.10	IL-MeOH- H ₂ O	7.00	>99	91	20	-
8	-1.00	IL-MeOH- H ₂ O	13.00	>99	>99	87	-
9	-1.00	IL-MeOH- H ₂ O	1.00	>99	94	19	53
10	-1.00	IL-MeOH- H ₂ O	0.60	>99	88	4	60
11	-1.00	IL-MeOH- H ₂ O	0.30	>99	98	<1	70
12	-1.00	IL-MeOH- H ₂ O	0.00	>99	94	18	42
13	-0.80	IL-MeOH- H ₂ O	0.30	>99	82	20	11
14	-0.90	IL-MeOH- H ₂ O	0.30	>99	80	6	19
15	-1.10	IL-MeOH- H ₂ O	0.30	>99	89	1	4
16	-1.00	MeOH- H ₂ O (Saturated KClO ₄)	7.00	82	75	80	1
17	-1.00	MeOH- H ₂ O (Saturated KClO ₄)	0.30	97	86	71	11

ⁱThe reference electrode is Ag/AgCl (3.5 M KCl), and all potentials were converted to the reversible hydrogen electrode (RHE) scale. ⁱⁱThe anolytes were 0.1 M NaOH (pH = 13.00), 0.5 M Na₂SO₄ (pH = 7.00), 0.1 M H₂SO₄ (pH = 1.00), 0.25 M H₂SO₄ (pH = 0.60), 0.5 M H₂SO₄ (pH = 0.30), and 1.0 M H₂SO₄ (pH = 0.00), with an error of ±0.05. ⁱⁱⁱThe results were qualitatively analyzed by GC-MS and quantitatively determined by HPLC using the external standard method. Reaction conditions: constant potential control, H-cell, 12 h. Pd₃₀Ni₅₀P₂₀ MG cathode, RuO₂-IrO₂/Ti mesh anode. Catholytes: 5 mM 2-PAP in 14.25 mL [Emim][BF₄]-cosolvents (binary, 1:1, v/v; ternary, 1:1:1, v/v/v), anolytes: different aqueous solutions. The potential values are not iR-corrected.

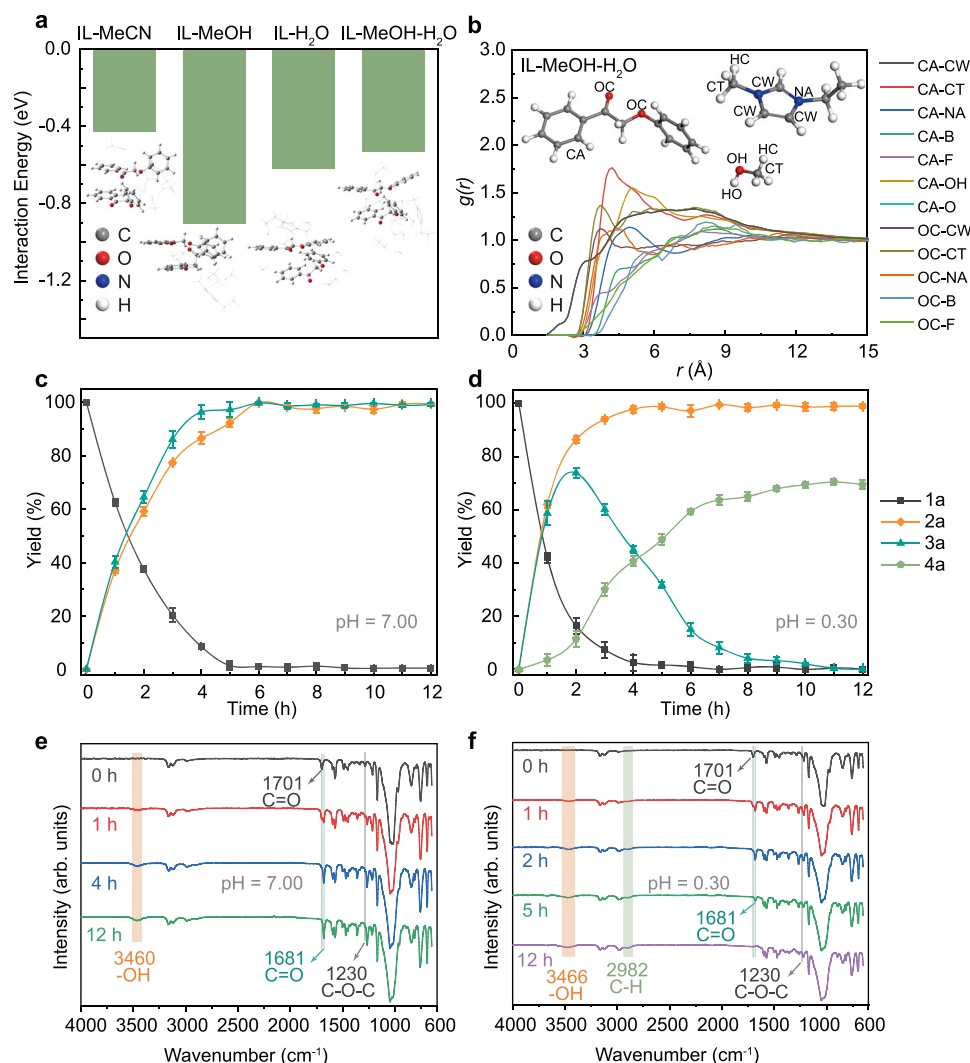


Fig. 4 | Optimization of electrolytes and tuning of product selectivity in electroreduction experiments. **a** The interaction energy between two 2-PAP molecules in four different electrolytes. The inset images illustrate the molecular structures and interactions within each electrolyte environment. **b** The radial distribution function (RDF, $g(r)$) of the atom pairs of the C/O atom in lignin to the C/N/B/F/O/H atoms in the cation, anion, MeOH, and H₂O. The insert shows the labeled atoms. The 12-hour reaction-time curves with analytes at **c** pH = 7.00 and **d** pH = 0.30. Error bars represent standard deviation, $n = 3$ independent

measurements at each pH value. FTIR spectra of catholytes at different electroreduction times with analytes at **(e)** pH = 7.00 and **(f)** pH = 0.30. Reaction conditions: H-cell, 12 h, $-1.00 V_{RHE}$, a three-electrode system with a Pd₃₀Ni₅₀P₂₀ MG cathode as the working electrode, a RuO₂-IrO₂/Ti mesh anode, and an Ag/AgCl reference electrode, with all potentials converted to the RHE scale. Catholytes: 5 mM 2-PAP in 14.25 mL [Emim][BF₄]-MeOH-H₂O (1:1, v/v/v), analytes: 0.5 M Na₂SO₄ (pH = 7.00) and 0.5 M H₂SO₄ (pH = 0.30), with a pH error of ± 0.05 . The potential values are not iR-corrected. Source data for Fig. 4 are provided as a Source Data file.

provides hydrogen protons during the electroreduction process (Supplementary Fig. 16). DFT calculations indicate a favorable interaction energy of -0.534 eV in the ternary electrolyte (Fig. 4a), elucidating the enhanced lignin dissolution observed. Molecular Dynamics (MD) simulations provide further insights, demonstrating that the improved dissolution is primarily due to the strong interactions between the carbon atoms on the lignin benzene ring and those present in the methyl and methylene groups of the cation and MeOH (Fig. 4b and Supplementary Fig. 17). The reaction voltage was optimized based on the CV curve of 2-PAP in the ternary electrolyte, with E_{p1} at $-0.86 V_{RHE}$ and E_{p2} at $-1.08 V_{RHE}$. Degradation is sluggish and incomplete at voltages below E_{p1} (Table 1, entry 5), while the yield of **3a** significantly declines at voltages above E_{p2} (Table 1, entry 7), suggesting that higher reduction voltages may cause undesirable condensation of **3a**. A series of electroreduction experiments revealed that $-1.00 V_{RHE}$ maximizes both conversion and product yield (Table 1, entry 4, and Fig. 4c). Finally, various IL systems were explored based on the optimized ternary electrolyte system (Supplementary Table 1). The

degradation results indicate that the [Emim][BF₄] exhibits the highest substrate conversion and product yield, likely due to its high conductivity, facilitating charge transfer and enhancing the overall catalytic effect.

Electrocatalytic hydrogenation

As is well known, depolymerization and hydrogenation occur simultaneously in electroreduction experiments. A significant challenge in hydrogenation is maintaining the aromaticity of degradation products while avoiding over-hydrogenation. To address this, we adjusted the pH of the anolyte (Table 1, entries 8–12), and it was discovered that 2-PAP can be completely degraded at various pH values, yielding high amounts of **2a**. Surprisingly, as the acidity of the anolyte increases, **3a** undergoes gradual hydrogenation to form a new product, 1-phenylethanol (**4a**), while maintaining its aromaticity. Complete hydrogenation of **3a** is achieved at a pH of 0.30, with **4a** being formed in a 70% yield. Deviating from this optimal pH, either by lowering or increasing it, results in reduced hydrogenation efficiency. It is

important to note that electroreduction experiments using acidic electrolytes at the cathode lead to a significant decrease in the yield of **4a**, due to the preferential occurrence of HER over substrate depolymerization (Supplementary Table 2 and Supplementary Fig. 18). To explore the formation pathway of **4a**, hydrogenation experiments were carried out on **3a** under the same conditions. Complete conversion of **3a** to **4a** is achieved, with a yield of 68%, essentially mirroring the hydrogenation yield of 2-PAP. This confirms that **4a** is derived from further hydrogenation of **3a** (Supplementary Fig. 19a).

Next, we investigated the effect of voltage on hydrogenation performance. The optimal working voltage under acidic anolytes is found to be similar to that under neutral anolytes, with the highest yield achieved between two reduction peaks (Table 1, entries 13–15). At $-1.00 V_{RHE}$, the yield of **4a** is 3.7 times higher than that at the lower voltage of $-0.90 V_{RHE}$, and 16 times higher than that at the higher voltage of $-1.10 V_{RHE}$ (Supplementary Fig. 19b). These results indicate that reduction voltages below E_{p1} limit the hydrogenation efficiency while voltages near E_{p2} promote the dimerization of **3a**, thereby reducing the yields of both **3a** and **4a**. The reaction-time curve of 2-PAP at $-1.00 V_{RHE}$ and pH 0.3 (Fig. 4d) shows that almost 50% of the substrate is converted within 1 hour, with the yield of **3a** peaking at 72% after 2 hours. Subsequent hydrogenation converts **3a** to **4a** with a final yield of 70%. Notably, the aromatic ring of **4a** is maintained under continuous electroreduction.

In situ infrared spectroscopy was used to further elucidate the depolymerization process. As shown in Fig. 4e, under neutral anolytes, the characteristic vibrational peak of the C–O–C ether bond at 1230 cm^{-1} in the substrate gradually decreases as the reaction progresses, accompanied by the appearance of characteristic peaks for **3a** (1681 cm^{-1}) and **2a** (3460 cm^{-1}). Under acidic anolytes, the vibrational peak of **3a** begins to attenuate after 5 h, coinciding with the appearance of the characteristic C–H vibrational peak of **4a** (2982 cm^{-1}), confirming the hydrogenation of **3a** to **4a** (Fig. 4f). These observations are consistent with the reaction pathway depicted in Fig. 4c and d, where C–O bond cleavage is followed by a hydrogenation reaction. Compared to previous investigations, this electrocatalytic system adeptly circumvents the common pitfalls of monomer repolymerization and excessive hydrogenation, which are typically encountered in lignin hydrogenation processes^{26,50}, paving the way for the high-value utilization of lignin.

Additionally, ensuring the stability of IL electrolytes is critical for the long-term operation of electrocatalytic systems. Fourier Transform Infrared Spectroscopy (FTIR) was employed to assess this stability (Supplementary Fig. 20). After electroreduction, the [Emim][BF₄] IL was separated from the post-electrolysis solution, and the resulting spectra are found to be entirely consistent with the pre-electrolysis spectra, directly confirming the stability of the IL as an electrolyte throughout the process.

Substrate scoping

To evaluate the versatility of the electrocatalytic system, eight substrates with methoxy substitutions on both the benzene and phenol rings (**1a–1h**, see Fig. 5, Supplementary Table 3 and Supplementary NMR Spectra) were selected for testing. A 12-hour electroreduction experiment under neutral anolytes (Supplementary Fig. 15b) revealed that the degradation primarily occurs within the first 4 hours and is completed within 6 hours. The final product yields, **2a–2h**, and **3a–3h**, all exceed 90% (Supplementary Figs. 21–29), demonstrating the high activity of the electrocatalytic system for lignin depolymerization. From the conversion results (Supplementary Fig. 15c, d), it is observed that introducing methoxy groups at the R4 positions (yielding **1b**) significantly accelerates the conversion rate. In contrast, the additional introduction of a methoxy group at the R3 position (as seen in **1c**) leads to a decreased conversion rate. These results suggest that during the adsorption process, the benzene ring is more favorably adsorbed on the catalyst surface

than the phenol ring. Consequently, methoxy substitutions on the benzyl-benzene ring hinder substrate adsorption due to increased steric hindrance, thereby reducing the conversion rate. Further analysis showed that the substitution effect on electroreduction depends not only on the positions but also on the number of substitutions, with fewer substitutions corresponding to faster conversion rates.

Under acidic anolytes, tandem hydrogenation contributes to the formation of alcohol products, with the hydrogenation yield strongly influenced by the position of the substituents (Fig. 5 and Supplementary Figs. 30–38). Substituents on the phenol ring exert no considerable impact on hydrogenation efficacy (**1b**). In contrast, those positions on the benzyl benzene ring markedly suppress the hydrogenation process, culminating in a diminished production of alcohols. Specifically, substitutions at the R1 and R3 positions (**1c**, **1e**, **1g**, **1h**) are associated with a significant presence of ketones, despite an equally low yield of hydrogenation products. This implies that the hydrogenation of ketones is hindered, which in turn leads to a reduced alcohol yield. Conversely, substitution at the R2 position (**1f**) results in a decreased ketone yield, implying that the lack of hydrogenation products may be due to the conversion of ketones into other types of products. These findings underscore the intricate influence of substituent positioning on hydrogenation reactions, warranting further investigation in future studies.

Electroreduction mechanism

To gain deeper insights into the performance of the Pd₃₀Ni₅₀P₂₀ MG catalyst, its degradation effects were compared with those of crystalline Pd₃₀Ni₅₀P₂₀ (Supplementary Fig. 39) and Pd/C catalysts. The MG catalyst exhibits superior selectivity for both **3a** and **4a**, while simultaneously maintaining a high yield of **2a** across different anolyte environments (Fig. 6a). Under neutral anolyte conditions, the MG catalyst achieves nearly 100% selectivity for **3a**. In comparison, the crystalline catalyst experiences a substantial reduction in **3a** selectivity to approximately 20%, along with a slight decline in the yield of **2a**. Though the Pd/C catalyst shows high selectivity for **3a**, the overall product yield is considerably lower. In acidic anolytes, the MG catalyst facilitates the complete hydrogenation of **3a** to **4a**, while the Pd/C catalyst only achieves partial hydrogenation, likely influenced by the morphology and hydrophilicity of the carbon substrate. Additionally, although the crystalline catalyst matches the selectivity of the MG catalyst for **4a**, it suffers from a low yield of **2a**. Previous studies have shown that Ni plays a crucial role in activating and cleaving the C–O ether bonds, while Pd helps to inhibit the over-hydrogenation of aromatic rings^{26,38,50–52}. By carefully combining Pd with Ni, electron transfer between these two metals (Fig. 2d) neutralizes their individual reductive abilities, improving the selectivity for aromatic products.

To elucidate the superior catalytic performance of the amorphous catalyst, DFT calculations were performed, and an electroreduction mechanism was proposed based on our earlier studies³⁸ (Fig. 6b). In a neutral anolyte, the reaction primarily involves the C–O bond cleavage, while in an acidic anolyte, the cleavage is followed by hydrogenation of the ketone product due to an increased hydrogen source availability. Specifically, in a neutral anolyte, the adsorbed substrate **1a** gains electrons to form the radical anion **1a'**, which decomposes into the radical **3a'** and the phenol anion. Protons from the environment are then captured, yielding the final products **2a** and **3a**, which subsequently desorb from the electrode. In an acidic anolyte, **2a** desorbs, and **3a** gains additional electrons to form the radical anion **4a'**. Through hydrogenation and desorption, **4a** is ultimately produced. Radical quenching experiments confirm the involvement of radicals in the reaction process, as detailed in Supplementary Table 4. Figure 6c presents the calculated adsorption energies for crystalline and MG catalysts. The crystalline catalyst shows an adsorption energy of -0.86 eV between Ni and the substrate, whereas the MG catalyst displays a more negative adsorption energy of -2.96 eV , underlining the superior substrate adsorption ability of the MG catalyst

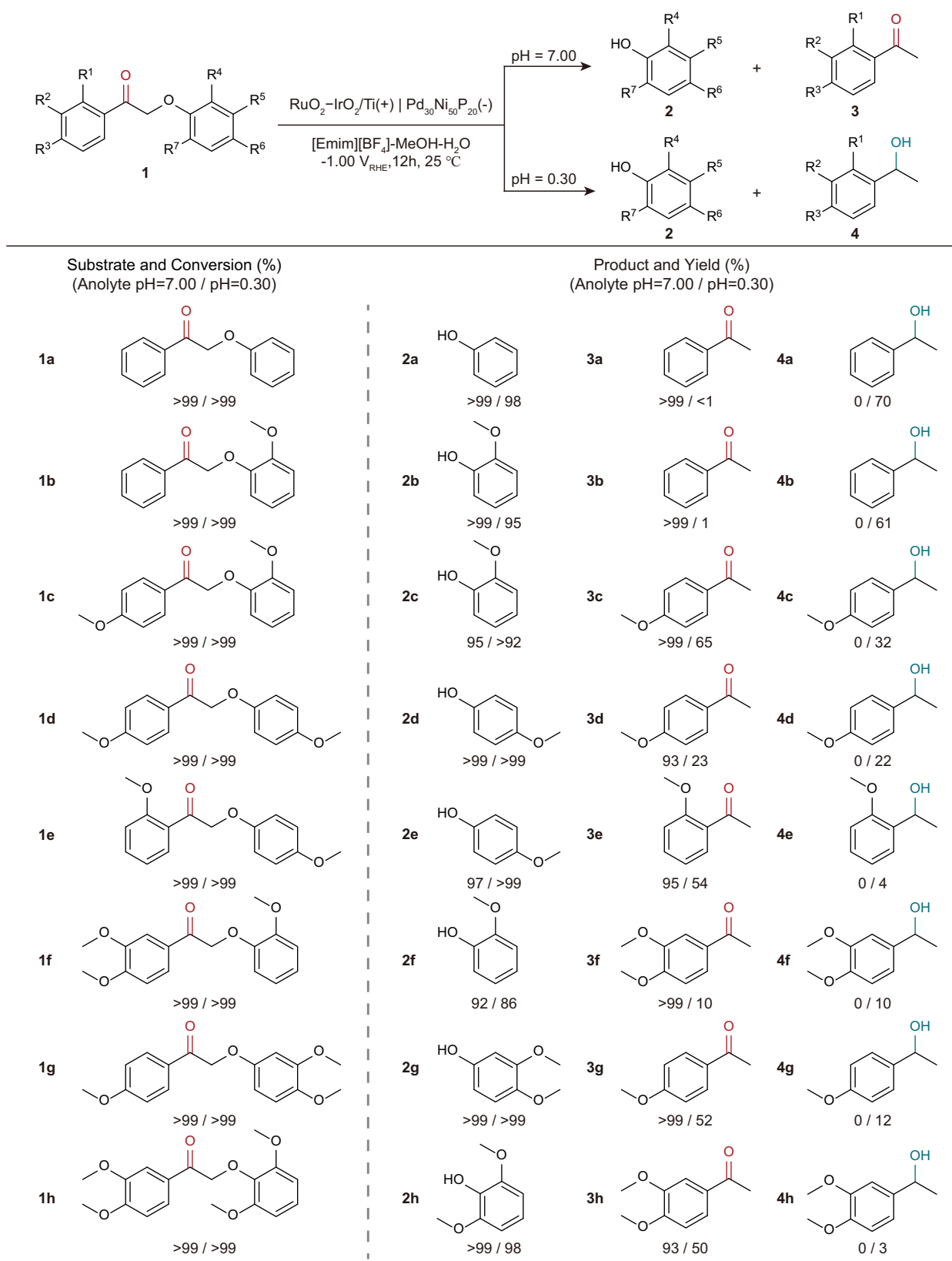


Fig. 5 | Substrate scope of lignin model compounds. Reaction conditions: H-cell, 12 h, -1.00 V_{RHE}, a three-electrode system with a Pd₃₀Ni₅₀P₂₀ MG cathode as the working electrode, a RuO₂-IrO₂/Ti mesh anode, and an Ag/AgCl reference electrode, with all potentials converted to the RHE scale. Catholytes: 5 mM 2-PAP in

14.25 mL [Emim][BF₄]-MeOH-H₂O (1:1:1, v/v/v), anolytes: 0.5 M Na₂SO₄ (pH = 7.00) and 0.5 M H₂SO₄ (pH = 0.30), with a pH error of ±0.05. The potential values are not iR-corrected. Source data for Fig. 5 are provided as a Source Data file.

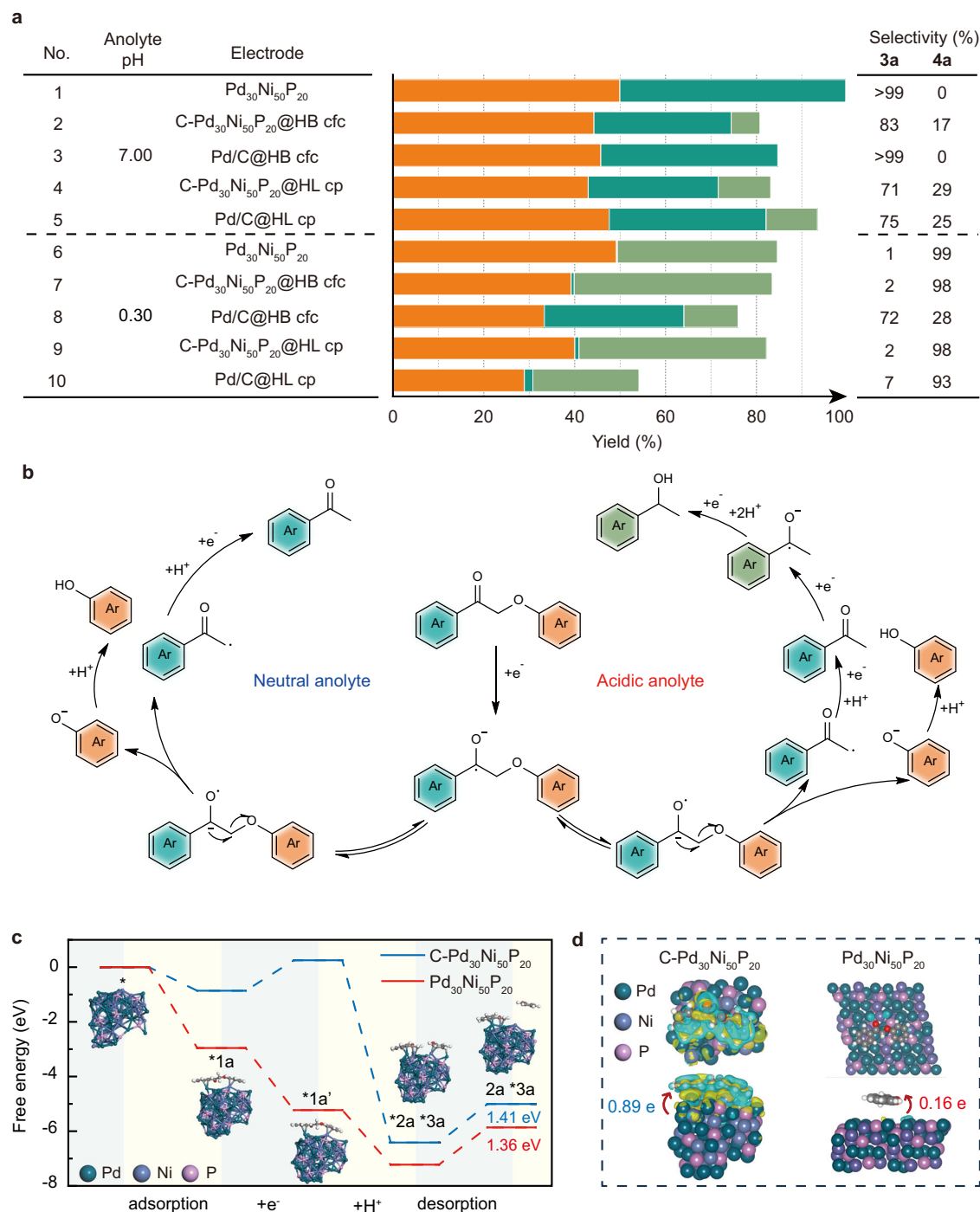


Fig. 6 | Electroreduction mechanism. a The product distribution of **1a** electroreduction under different catalysts (HL cp: hydrophilic carbon paper, HB cfc: hydrophobic carbon fiber cloth, C-Pd₃₀Ni₅₀P₂₀: crystalline Pd₃₀Ni₅₀P₂₀). **b** Electroreduction mechanism of **1a** under neutral and acidic anolytes. **c** The free energy curve for **1a** electroreduction by amorphous and crystalline Pd₃₀Ni₅₀P₂₀ catalysts. **d** Distributions of the charge density difference for **1a** adsorbed on amorphous and crystalline Pd₃₀Ni₅₀P₂₀ catalysts. Reaction conditions: H-cell, -1.00

V_{RHE}, 12 h, a three-electrode system with a Pd₃₀Ni₅₀P₂₀ MG cathode (No. 1, 6) or carbon cloth-supported catalysts with the loading of 5.0 mg cm⁻² (No. 2-5, 7-10) as the working electrode, a RuO₂-IrO₂/Ti mesh anode, and an Ag/AgCl reference electrode, with all potentials converted to the RHE scale. Catholytes: 5 mM 2-PAP in 14.25 mL [Emim][BF₄]-MeOH-H₂O (1:1:1, v/v/v), anolytes: 0.5 M Na₂SO₄ (pH = 7.00) and 0.5 M H₂SO₄ (pH = 0.30) with a pH error of ±0.05. The potential values are not iR-corrected. Source data for Fig. 6a, c are provided as a Source Data file.

(Supplementary Figs. 40 and 41). Charge transfer analysis during the adsorption process reveals that the crystalline catalyst facilitates a charge transfer of 0.16e, whereas the MG catalyst enables a much higher charge transfer of 0.89e (Fig. 6d). For the rate-determining step of **2a** desorption, the energy required for the crystalline catalyst is 1.41 eV, while for the MG catalyst only needed 1.36 eV. This lower energy barrier indicates that the MG catalyst promotes **2a** desorption

and exposes more catalytically active sites for the subsequent hydrogenation reaction. The DFT calculation results, to some extent, uncovered the superior performance of the MG catalyst¹⁰.

Electroreduction of real lignin

The electroreduction method was extended to real lignin using natural birch wood as a model. The extracted lignin was first oxidized to

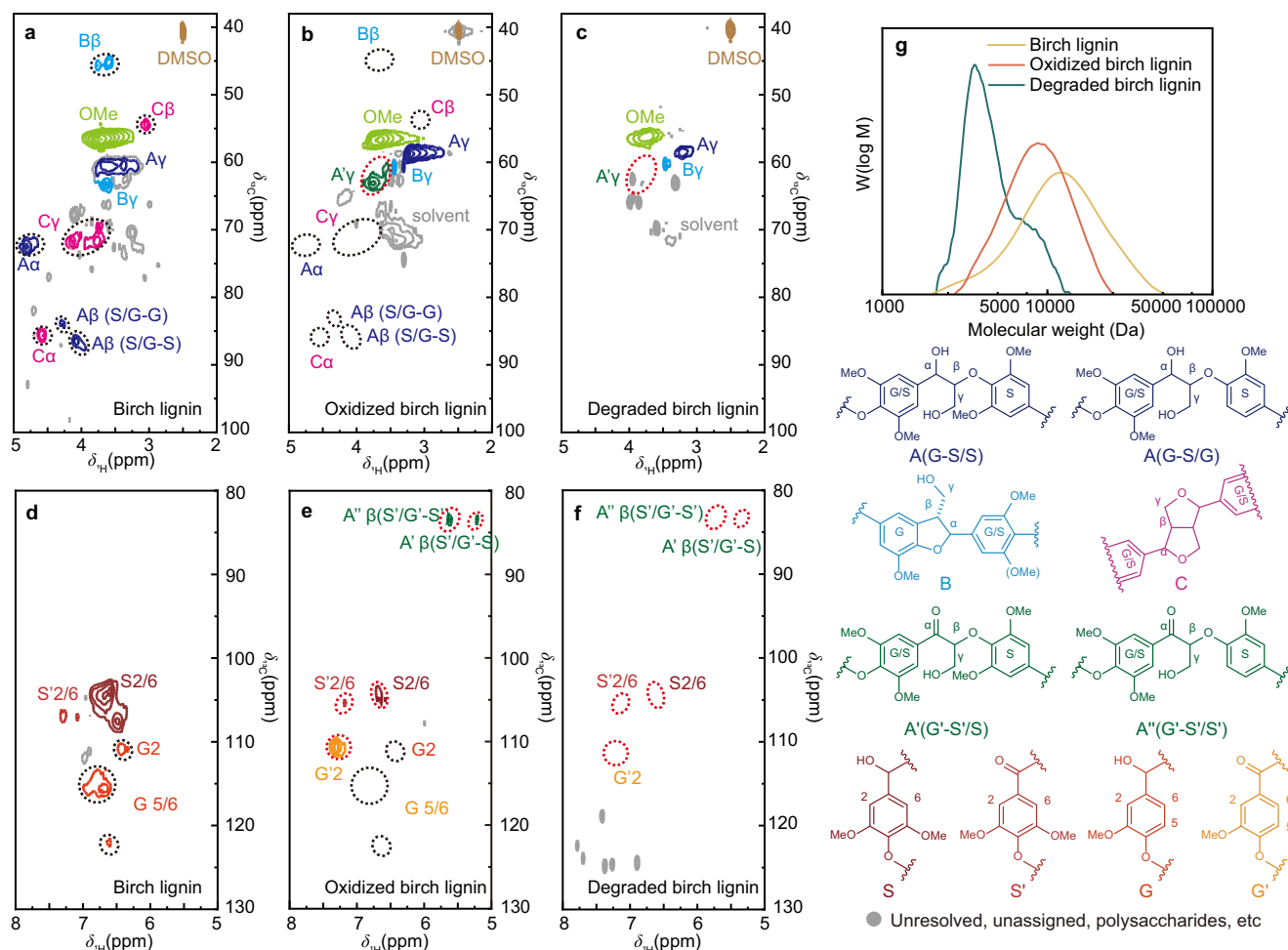


Fig. 7 | 2D HSQC NMR and GPC characterization of the birch lignin before and after oxidation and electroreduction. a–c Oxygenated regions and **d–f** aromatic regions of the 2D HSQC NMR spectra. The left column: extracted lignin, the middle column: oxidized lignin, and the right column: degraded lignin. **g** GPC curves for extracted, oxidized, and degraded birch lignin. Reaction conditions: H-cell, -1.00 V_{RHE}, **12 h**, a three-electrode system with a Pd₃₀Ni₅₀P₂₀ MG cathode as the working

electrode, a RuO₂-IrO₂/Ti mesh anode, and an Ag/AgCl reference electrode, with all potentials converted to the RHE scale. Catholytes: 2 g L^{-1} oxidized birch lignin in 14.25 mL [Emim][BF₄]-MeOH-H₂O (1:1:1, v/v/v), anolytes: 0.5 M Na₂SO₄ (pH = 7.00), with a pH error of ± 0.05 . The potential values are not iR-corrected. Source data for Fig. 7 g are provided as a Source Data file.

increase the C α =O content in the lignin structure, following a previously reported procedure⁵³. The 2D HSQC NMR spectra (Fig. 7a, d) confirm the presence of key lignin linkages, including β -O-4 (A), β -5(B), and β - β (C) linkages. Post-oxidation spectra (Fig. 7b, e) revealed the expected changes: the disappearance of the A β linkage, the emergence of α -keto groups (A' β and A'' β), and the disappearance of G2 and G5/6 signals, with the appearance of G'2. These spectral changes confirm the successful oxidation of C α -OH to C α =O.

The oxidized birch lignin was subsequently subjected to electroreduction using the Pd₃₀Ni₅₀P₂₀ catalyst. The resulting spectra (Fig. 7c, f) clearly depict the absence of A β , A' β , and A'' β , and S2/6, S'2/6, and G'2 signals, suggesting the effective cleavage of C-O bonds. The effectiveness of lignin electroreduction was further evidenced by the GPC chromatograms. Although the oxidized lignin exhibits a decreased molecular weight compared to the initially extracted lignin, which is echoed by the disappearance of A α , B β , and C γ in the 2D HSQC NMR spectra, a more pronounced decrease in molecular weight is observed after electroreduction (Fig. 7g and Supplementary Table 7). These results indicate that electroreduction is more effective in breaking down the polymeric structure of lignin than oxidation alone, yielding a higher proportion of low-molecular-weight components. Product analysis following electroreduction confirm the generation of various

aromatic products, with vanillic acid achieving a yield of 8 wt% (Supplementary Fig. 42). In contrast, under acidic anolytes, no aromatic products are detected, likely due to the precipitation of lignin during the degradation process. Further investigations will be required to optimize the degradation of real lignin under acidic anolyte conditions (Supplementary Figs. 43, 44).

Discussion

In summary, we have developed an efficient electrocatalytic system that enables selectively direct lignin electroreduction from depolymerization to hydrogenation. The amorphous MG catalyst, combined with the IL electrolyte, achieves the complete cleavage of the β -O-4 bonds in lignin model compounds. By adjusting the anolyte from neutral to acidic conditions while keeping other reaction parameters identical, ketone products are effectively hydrogenated to alcohol products without compromising aromaticity, while the yield of phenolic products remains consistently high throughout the process. Mechanistic studies uncover that the amorphous feature of the catalyst significantly enhances substrate adsorption and facilitates product desorption, contributing to its superior catalytic performance compared to its crystalline counterpart. More importantly, the MG ribbon catalyst exhibits remarkable stability, maintaining both its structure

and catalytic activity over 100 electrocatalytic cycles, and works well with real lignin, suggesting strong potential for practical applications in lignin valorization. The insights gained from this study offer valuable guidance for designing high-performance electrocatalysts and controlling product selectivity in the electroreduction of lignin. By fine-tuning the electrolyte composition, we can strategically influence reaction pathways, paving the way for the efficient production of high-value chemicals from lignin.

Methods

Materials

All solvents and reagents were purchased from commercial suppliers and used as received unless otherwise stated. Ionic liquids were dried under vacuum at 70 °C for 48 h before use. Deionized water was sourced from Wahaha Purified Water. RuO₂–IrO₂/Ti mesh, Nafion-117 membrane, carbon-based electrodes, and electrochemical cells were obtained from specialized suppliers. Birch wood was sourced from Heilongjiang, China. Detailed information regarding the purity and sources of reagents and materials is provided in the Supporting Information.

Preparation of the catalyst

Pd (99.99%) and Ni (99.99%) were melted under argon to form Pd–Ni alloy ingots, which were then combined with P (99.5%) to form Pd₃₀Ni₅₀P₂₀, Pd₄₀Ni₄₀P₂₀, and Pd₅₀Ni₃₀P₂₀ (in atomic percentage). This alloy was mixed with a large volume of B₂O₃ (2 to 3 times the volume of the alloy) and annealed at 1000 °C for 10 hours. Finally, Pd–Ni–P ribbons were produced by melt-spinning in argon, using copper rollers to obtain ribbons with the rollers spinning at 60 m s^{−1}.

Catalyst characterization

Structural characterization was conducted using a field-emission scanning electron microscope (SEM) model SU8020. Elemental content determination was facilitated by energy dispersive spectrometry (EDS, X-MaxN50 Aztec). The crystal structure of the catalyst was determined by X-ray diffraction (XRD) with an X'PERTPRO MPD diffractometer using Cu K α radiation (λ = 0.15406 nm). Surface composition was determined through X-ray photoelectron spectroscopy (XPS), using an ESCALAB 250Xi spectrometer equipped with a 75–150 W Al K α cathode source under ultrahigh vacuum conditions. Calibration of all raw XPS spectra was performed with the C 1s line at 284.80 eV. The thermal stability of MG ribbons was measured by TG-DTA6300 thermogravimetric differential thermal analyzer at a heating rate of 10 K min^{−1} under the N₂ atmosphere. The HRTEM sample was prepared using a focused ion beam (FIB) approach and HRTEM was performed on a JEM-2100(UHR) microscope operating at 200 kV. Synchrotron small- and wide-angle X-ray scattering (SAXS–WAXS) measurements were conducted at the Beijing Synchrotron Radiation Facility using a 1.54 Å wavelength. Data were collected with Pilatus 1M and SX 165 CCD detectors^{54,55}. XAFS spectra at the Pd K-edge were collected at BL14W1 station in Shanghai Synchrotron Radiation Facility (SSRF), operating at 3.5 GeV with a maximum current of 250 mA. At BL14W1, the X-ray beam was monochromatized using a Si (311) double-

crystal monochromator. The incident X-ray intensity was monitored by an Ar-filled ion chamber (IO) placed in front of the sample. Solid samples were mounted in an aluminum sample holder and sealed with kapton tape. Fluorescence excitation spectra were recorded using a Lytle detector. The acquired EXAFS data were processed following standard procedures using the ATHENA and ARTEMIS modules in the IFEFFIT software package. Fourier Transform Infrared Spectroscopy (FTIR) was conducted using a Thermo Scientific Nicolet iS50 in the range of 4000–600 cm^{−1}. Due to the overlap of functional groups in H₂O and MeOH, which are present in the ternary electrolyte, with those of the electroreduction products in the FTIR spectra, accurate analysis was challenging. To resolve this, the electrolyte was subjected to rotary evaporation at different reaction times to remove water and methanol prior to FTIR characterization.

Preparation of the working electrode

The MG ribbon (width: 0.8 mm, thickness: 0.015 mm) was wrapped around a custom-designed quartz plate to serve as the working electrode, yielding an effective length of approximately 160 mm (Supplementary Fig. 2). This electrode configuration remained unchanged throughout all experimental procedures to ensure consistency.

Crystallized Pd₃₀Ni₅₀P₂₀ catalysts were synthesized by annealing the MG ribbons at 400 °C for 2 h under argon atmosphere, with the resultant crystalline structure verified by XRD (Supplementary Fig. 39). The annealed sample was ground into powder (7.0 mg), which was then mixed with 100 μ L 5 wt% Nafion, 250 μ L ethanol, and 650 μ L deionized water. After 30 min of ultrasonic homogenization, the slurry was uniformly coated onto a pretreated substrate (0.7 \times 20 mm) and air-dried overnight at 25 °C. The identical protocol was applied to prepare the Pd/C catalyst for comparative studies.

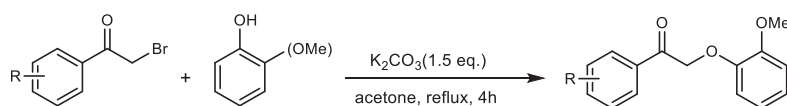
An Ag/AgCl reference electrode (3.5M KCl, Luggin capillary-equipped) was calibrated against a standard hydrogen electrode (SHE) in 1M HCl solution at 25 °C. The measured potential exhibited a deviation within ± 5 mV from the theoretical value (+0.205 V vs. SHE). All electrochemical potentials were recorded against this calibrated reference electrode and subsequently converted to the reversible hydrogen electrode (RHE) scale using Eq. (1):

$$E_{\text{RHE}} = E_{\text{Ag/AgCl}} + 0.059 \times \text{pH} + E_{\text{Ag/AgCl}}^0 \quad (1)$$

where $E_{\text{Ag/AgCl}}^0$ represents the standard electrode potential versus SHE at 25 °C.

Preparation of the lignin model compounds

A 250 mL round bottom flask equipped with a reflux condenser and a dropping funnel was charged with phenol (12.6 mmol, 1.26 eq.) and K₂CO₃ (2.07 g, 15.0 mmol, 1.50 eq.) in acetone (50.0 mL) and stirred at room temperature. To this solution, 2-bromoacetophenone (10.0 mmol, 1.00 eq.) in acetone (50.0 mL) was added dropwise over 30 min at room temperature. The resulting suspension was stirred at reflux for 4 h. Afterward, the suspension was filtered and concentrated in vacuo. The crude product was purified by recrystallization from ethyl acetate/cyclohexane (1:3, v/v) to obtain the product.



Extraction and oxidation of birch lignin

The extraction and oxidation process of birch wood lignin was optimized based on previous studies. Birch wood was debarked, pulverized, and sieved through a 60-mesh screen before drying. 40 g of the wood powder was mixed with 288 mL of 1,4-dioxane and 32 mL of 2 N HCl and refluxed at 120 °C under nitrogen for an hour. After cooling and filtering, the filtrate was vacuum-concentrated into a gel-like residue, dissolved in 45 mL acetone and 5 mL water, then precipitated into 500 mL water, yielding crude lignin upon filtration and drying. This was redissolved in 45 mL acetone and 5 mL MeOH and precipitated in 400 mL ether for purification. The process resulted in approximately 4.3 g of purified birch lignin.

For lignin oxidation: 0.3 g DDQ and 346 μ L tBuONO were added to the lignin (2 g) in a 2-methoxyethanol/1,2-dimethoxyethane mixture (2:3, v/v, 14 mL g⁻¹). The mixture was stirred under an oxygen atmosphere at 80 °C for 14 hours. The oxidized lignin was precipitated in ether, filtered, and dried under vacuum to yield approximately 1.8 g of purified product, ready for use without further treatment.

Electrochemical measurements

The conductivity of the MG ribbons was measured using a digital multimeter (Fluke 289 °C). The electrical conductivity and viscosity of the catholytes were measured at room temperature using a Mettler Toledo FE30 conductivity meter and a DMA5000M-Lovis2000Mem density-viscosity meter, respectively. Electrochemical assessments were conducted in a three-electrode H-cell, equipped with a Pt wire counter electrode and an Ag/AgCl reference electrode. Cyclic Voltammetry (CV) and Linear Sweep Voltammetry (LSV) analyses were executed on a PARSTAT3000A-DX (Princeton Instruments, Inc., USA) electrochemical workstation, with scan rates of 0.05 V s⁻¹ and 0.005 V s⁻¹, respectively. Electrochemical Impedance Spectroscopy (EIS) measurements were performed using a CHI 660D (CH Instruments, Inc, Shanghai) workstation at -1.00 V_{RHE}, spanning frequencies from 1 \times 10⁵ to 0.01 Hz with an amplitude of 5 mV.

Electroreduction experiments

The electrochemical measurements were performed using a Princeton PARSTAT 3000A-DX bipotentiostat with a current range was 200 mA, and a voltage range was \pm 6 V. Chronoamperometry tests were conducted at fixed potentials versus the Ag/AgCl reference electrode, with raw current-time data acquired at a sampling interval of 0.02 s for 43,200 s (12 h). No iR compensation was applied and the raw data were used directly without any processing.

A three-electrode H-cell separated by a pretreated Nafion-117 membrane (thickness: 183 μ m; diameter: 30 mm; ion exchange capacity: 0.89 meq·g⁻¹; geometric details in Supplementary Fig. 1b) served as the electrochemical reactor. Before use, the Nafion-117 membrane underwent sequential pre-treatment in 5% H₂O₂ (80 °C, 1 h), deionized water (25 °C, 0.5 h), 5% H₂SO₄ (80 °C, 1 h), and deionized water (25 °C, 0.5 h), then was stored in deionized water until use. The reference electrode was Ag/AgCl, and the counter electrode was RuO₂ - IrO₂/Ti (15 \times 30 mm). Both the working and counter electrodes were secured using Pt electrode clips.

Prior to each electrocatalytic test, 15 mL of ionic liquid (IL)-based electrolyte was freshly formulated. The total volume was partitioned into two fractions: 0.75 mL for Luggin capillary filling and 14.25 mL as the catholyte base. To the base electrolyte, 5 mM lignin model compound was introduced under magnetic stirring (800 rpm, 25 °C, 10 min), followed by 1 min ultrasonication to eliminate dissolved gases. The resulting catholyte pH was determined via triplicate measurements using a calibrated INESA PHS-25 pH meter, with the mean value reported with a standard deviation.

Throughout the electrocatalytic process, 250 μ L aliquots were collected hourly via a syringe, diluted to 1 mL with HPLC-grade MeOH for high-performance liquid chromatography (HPLC). Upon reaction

completion, 1 mL of the catholyte was acidified to pH 3.00-4.00 using 0.5 M H₂SO₄ for gas chromatography-mass spectrometry (GC-MS).

The electroreduction protocol was extended to oxidized birch lignin (2 g L⁻¹) following identical operational parameters as model compounds. The recovery and characterization of the IL, as well as the methods for the separation and purification of the products are provided in the supplementary information.

Isolation of the products derived from oxidized birch lignin

After the reaction, the catholyte was added to twice its volume of deionized water, and the pH of the solution was adjusted to about 1 using 0.5 M H₂SO₄ to precipitate the unreacted lignin. After centrifugation, the solid was washed three times with deionized water and then dried in a vacuum oven at 60 °C for 24 hours to obtain the recovered undegraded lignin. Subsequently, the obtained solution was washed three times with an equal volume of ethyl acetate and dried with anhydrous Na₂SO₄ to obtain organic phase. After evaporating and concentrating, record the volume *V* and use it for GC-MS analysis. Drying enables ionic liquid recovery from the aqueous phase. The separated product of **1a**, together with the synthesized model compounds **1b-1h**, were characterized by one-dimensional proton nuclear magnetic resonance (¹H NMR) and ¹³C nuclear magnetic resonance (¹³C NMR) spectroscopy. The ¹H NMR spectra were recorded on a Bruker Avance III HD 600 instrument operating at 600 and 700 MHz, while the ¹³C NMR spectra were recorded on the same instrument at 151 and 176 MHz.

Recovery of the ionic liquid and product separation

After electroreduction, the catholyte was subjected to rotary evaporation at 40 °C to remove most of the H₂O and MeOH. To the remaining liquid phase, 4 mL of saturated NaCl solution and 10 mL of ethyl acetate were added, followed by thorough mixing. The lower aqueous phase was washed three times with 10 mL of ethyl acetate, and the organic phases were combined. The organic phase was dried over anhydrous Na₂SO₄, and then the ethyl acetate was removed by rotary evaporation. The product was dissolved in d-chloroform and analyzed by ¹H NMR spectroscopy. The aqueous phase was concentrated by rotary evaporation to remove most of the H₂O, followed by drying in a vacuum oven at 60 °C for 24 hours. The recovered ionic liquid was obtained by filtration.

Qualitative and quantitative analysis of electroreduction products

GC-MS analysis was performed using a Shimadzu GC-2030 system equipped with an Rx-5MS Ultra Inert capillary column (30 m \times 250 μ m \times 0.25 μ m) and an AOC-6000 Plus headspace sampler. For lignin model compounds, samples were heated at 170 °C for 1 min before being introduced via headspace injection with a split ratio of 10:1. For real lignin, the samples were directly injected after extraction and dehydration, with a split ratio of 50:1. The column temperature program was as follows: initial temperature 40 °C, held for 3 min, ramped to 80 °C at 10 °C min⁻¹, then to 120 °C at 5 °C min⁻¹, and finally to 240 °C at 15 °C min⁻¹, where it was held for 3 min, resulting in a total analysis time of 26 min. High-purity helium was used as the carrier gas at a flow rate of 1.0 mL min⁻¹. Mass spectrometric detection was conducted in the electron ionization (EI) mode, with an ion source temperature of 200 °C, an interface temperature of 250 °C, and a solvent delay time of 2 min. The scanning range was 35-500 m/z, with a scan interval of 0.30 sec.

For quantitative analysis of electroreduction products from lignin model compounds, HPLC (Prominence LC-20A) with a UV detector (SPD-20A) and C18 column (5 μ m, 250 \times 4.6 mm) was used. A MeOH-H₂O mixture served as the mobile phase at 0.5 mL min⁻¹ at 35 °C. Products were quantified at 254 nm using external standards. The substrate conversion ratio (*X*), product yield (*Y_i*), selectivity (*S_i*) and

faradaic efficiency (FE) were calculated according to Eqs. (2–5).

$$X = \frac{C_0 - C_t}{C_0} \times 100\% \quad (2)$$

$$Y_i = \frac{C_i}{C_0} \times 100\% \quad (3)$$

$$S_i = \frac{Y_i}{\sum Y_{\text{products}}} \times 100\% \quad (4)$$

$$\text{FE} = \frac{Z \times F \times \sum n_{\text{products}}}{Q} \times 100\% \quad (5)$$

Where C_0 , C_t and C_i represent the initial concentration, concentration at time t , and final concentration of product i , respectively. $\sum Y_{\text{products}}$ and $\sum n_{\text{products}}$ represent the cumulative yields of all products and the total mole amount of the product. Z , F , represent the electron transfer number and Faraday constant ($96\,485\text{ C mol}^{-1}$), respectively. Q represents the total charge consumed during the reaction.

The quantification of electroreduction products from real lignin was performed by GC-MS using an external standard method. The yield was calculated using Eq. (6):

$$Y_i = \frac{M_i V C_i}{m_{\text{lignin}^{\text{ox}}}} \times 100\% \quad (6)$$

where M_i represents the molar mass of product i , V represents the volume of the reaction mixture, C_i represents the concentration of product i , and $m_{\text{lignin}^{\text{ox}}}$ represents the mass of oxidized birch lignin added to the reaction. Both HPLC and GC-MS analyses were performed using the external standard method, with calibration curves constructed using standard compounds of known concentrations.

Characterization of the electroreduction products from oxidized birch lignin

Molecular weight profiles of lignin mixtures were determined by Gel Permeation Chromatography (GPC) on a Jasco HPLC 2000 (Groß-Umstadt) with a LaChrom Autosampler (Merck-Hitachi, Darmstadt), and Mixed-B Guard column (650 mm). Polystyrene standards were used for calibration. Samples were diluted in DMF for GPC measurement at 1.0 mL min^{-1} flow rate.

For HSQC NMR analysis, approximately 20 mg of lignin was dissolved in 500 μL DMSO- d_6 and examined using a Bruker Avance III HD 600 at 600 MHz (^1H) and 150 MHz (^{13}C). Data were acquired on a Bruker Avance 700 MHz spectrometer with a TCI-F cryoprobe, with spectral widths of 10.8261 ppm (^1H) and 165.0000 ppm (^{13}C), and 16 scans with a 1-second delay. Volume integration was performed with Bruker Topspin 3.5 pl4.

Simulation

To determine the binding energy between lignin and solvents, molecular dynamics (MD, Supplementary Data 1) simulations and Density Functional Theory (DFT, Supplementary Data 2) calculations were performed on a solvated lignin model. In MD simulation, lignin and solvent compositions (H_2O , MeOH, and MeCN) were based on experimental ratios (Supplementary Table 5). The radial distribution function (RDF) was analyzed to assess interactions between lignin and solvent atoms. Initial species configurations were generated using Packmol, and MD simulations were conducted with the OPLS-AA force field^{56,57}. Water molecules were modeled using the SPC/E model⁵⁸, while atomic charges for Coulombic interactions were obtained via the restrained electrostatic potential (RESP) method in Multiwfn^{59,60}. Each system underwent relaxation using the conjugate gradient algorithm,

followed by a 5 ns NPT run (300 K, 1 bar) with the Parrinello-Rahman barostat and equilibration in the NVT ensemble (300 K) using the Nose-Hoover thermostat until density and total energy stabilized ($\sim 20\text{ ns}$). A time step of 1 fs and a 12 Å cutoff for van der Waals (vdW) interactions were applied. An additional 3 ns production run was conducted for RDF analysis. All MD simulations were performed using LAMMPS⁶¹.

For the solubility evaluation of the lignin model compound in various electrolytes, the π - π interaction of the solvated model compound was optimized in an explicit solvent model using Gaussian 09⁶². The solvent compositions in DFT calculations are detailed in Supplementary Table 6. Geometry optimization was performed using the B3LYP-D3 functional with a 6-311 + G(d) basis set⁶³. Vibrational mode analysis confirmed the structures as true minima with zero imaginary frequency. The π - π interaction between two lignin model compounds was calculated by Eq. (5):

$$E_{\pi-\pi} = E_{\text{lignin_dimer}} - E_{\text{lignin_monomer1}} - E_{\text{lignin_monomer2}} \quad (5)$$

DFT calculations were carried out with the Vienna Ab initio Simulation Package (VASP), incorporating the projector augmented wave (PAW) method^{64–66}. Exchange-correlation interactions were treated with the Perdew-Burke-Ernzerhof (PBE) functional within the generalized gradient approximation (GGA)⁶⁷. A plane-wave cutoff energy of 500 eV and a $1 \times 1 \times 1$ gamma-centered k-point mesh were used. Van der Waals interactions were included via DFT-D3 correction⁶³. A 15 Å vacuum layer was added in the Z direction to prevent periodic image interactions. During relaxation, only the top two atomic layers were allowed to move, while the bottom layers remained fixed, and spin polarization was applied to Ni atoms. Convergence thresholds were set at 10^{-4} eV for energy and 0.10 eV \AA^{-1} for forces. Bader charges analysis and charge density difference evaluations were conducted using the Henkelman method and the VASPKIT toolkit^{68,69}.

For crystalline catalyst simulations, an orthorhombic supercell ($a = 3.47\text{ \AA}$, $b = 8.44\text{ \AA}$, $c = 6.61\text{ \AA}$) was constructed based on XRD data⁷⁰. The (112) crystallographic surface was selected, with atomic proportions adjusted accordingly. Amorphous $\text{Pd}_{30}\text{Ni}_{50}\text{P}_{20}$ structures were simulated using a cubic supercell containing 100 atoms in their respective ratios. The volume was optimized under zero external pressure. The system was equilibrated at 2000 K for 2000 steps, then cooled to 300 K over another 2000 steps, and finally optimized. Simulations used a 2 fs time step with an NVT ensemble controlled by a Nose thermostat.

Data availability

The source data underlying Figs. 2b, d–f, 3, 4, 5, 6a, c and 7g and Supplementary Figs. 3, 5, 6, 8–10, 12–15, 17–28, 30–37, 39 and 42 are provided as a Source Data file. The data that support the findings of this study are available from the corresponding author upon reasonable request. Source data are provided in this paper. Source data are provided with this paper.

References

- Fang, X., Kalathil, S. & Reisner, E. Semi-biological approaches to solar-to-chemical conversion. *Chem. Soc. Rev.* **49**, 4926–4952 (2020).
- Dragone, G. et al. Innovation and strategic orientations for the development of advanced biorefineries. *Bioresour. Technol.* **302**, 122847 (2020).
- Tan, T., Pang, S. & Zhang, Z. Editorial for special issue of biorefinery. *Biotechnol. Adv.* **37**, 507 (2019).
- Zhai, Z. et al. Recent advances in biomass-derived porous carbon materials: Synthesis, composition and applications. *Chem. Res. Chin. Univ.* **40**, 3–19 (2024).

5. Ralph, J., Lapierre, C. & Boerjan, W. Lignin structure and its engineering. *Curr. Opin. Biotechnol.* **56**, 240–249 (2019).
6. Dong, L. et al. Sustainable production of dopamine hydrochloride from softwood lignin. *Nat. Commun.* **14**, 4996 (2023).
7. Leng, E. et al. A comprehensive review on lignin pyrolysis: Mechanism, modeling and the effects of inherent metals in biomass. *Fuel* **309**, 122102 (2022).
8. Deng, W. et al. Catalytic conversion of lignocellulosic biomass into chemicals and fuels. *Green Energy Environ.* **8**, 10–114 (2023).
9. Luo, Z. et al. Catalytic hydrogenolysis by atomically dispersed iron sites embedded in chemically and redox non-innocent N-doped carbon. *J. Am. Chem. Soc.* **146**, 8618–8629 (2024).
10. Liu, X., Wang, Y. & Duan, H. Recent progress in electrocatalytic conversion of lignin: From monomers, dimers, to raw lignin. *Precis. Chem.* **2**, 428–446 (2024).
11. Wijaya, Y. P., Smith, K. J., Kim, C. S. & Gyenge, E. L. Electrocatalytic hydrogenation and depolymerization pathways for lignin valorization: Toward mild synthesis of chemicals and fuels from biomass. *Green Chem.* **22**, 7233–7264 (2020).
12. Cui, T. et al. Atomically dispersed Pt–N₃C₁ sites enabling efficient and selective electrocatalytic C–C bond cleavage in lignin models under ambient conditions. *J. Am. Chem. Soc.* **143**, 9429–9439 (2021).
13. Shao, D., Liang, J., Cui, X., Xu, H. & Yan, W. Electrochemical oxidation of lignin by two typical electrodes: Ti/SbSnO₂ and Ti/PbO₂. *Chem. Eng. J.* **244**, 288–295 (2014).
14. Gao, D., Ouyang, D. & Zhao, X. Electro-oxidative depolymerization of lignin for production of value-added chemicals. *Green Chem.* **24**, 8585–8605 (2022).
15. Zhou, Y. et al. Role of methoxy and C_α-based substituents in electrochemical oxidation mechanisms and bond cleavage selectivity of β-O-4 lignin model compounds. *Green Energy Environ.* **9**, 114–125 (2024).
16. Peng, T. et al. Ternary alloys enable efficient production of methoxylated chemicals via selective electrocatalytic hydrogenation of lignin monomers. *J. Am. Chem. Soc.* **143**, 17226–17235 (2021).
17. Lam, C. H. et al. Electrocatalytic upgrading of model lignin monomers with earth abundant metal electrodes. *Green Chem.* **17**, 601–609 (2015).
18. Garedew, M. et al. Electrochemical upgrading of depolymerized lignin: A review of model compound studies. *Green Chem.* **23**, 2868–2899 (2021).
19. Fang, Z., Jackson, J. E. & Hegg, E. L. Mild, electroreductive lignin cleavage: Optimizing the depolymerization of authentic lignins. *ACS Sustain. Chem. Eng.* **10**, 7545–7552 (2022).
20. Garedew, M. et al. Electrocatalytic cleavage of lignin model dimers using ruthenium supported on activated carbon cloth. *Sustain. Energ. Fuels* **4**, 1340–1350 (2020).
21. Yamamoto, Y. et al. Facile hydrogenative deprotection of N-benzyl groups using a mixed catalyst of palladium and niobic acid-on-carbon. *ACS Omega* **5**, 2699–2709 (2020).
22. Deng, J. et al. Visible-light-driven selective cleavage of C–C bonds in lignin model substrates using carbon nitride-supported ruthenium single-atom catalyst. *Chem. Eng. J.* **462**, 142282 (2023).
23. Halilu, A. et al. *Advanced heterogeneous catalysts volume 2: Applications at the single-atom scale* Ch. 5, 93–125 (American Chemical Society, Washington, DC, 2020).
24. Deng, W. et al. Oxidative conversion of lignin and lignin model compounds catalyzed by CeO₂-supported Pd nanoparticles. *Green Chem.* **17**, 5009–5018 (2015).
25. Wang, S., Li, X., Fu, C., Li, H. & Song, G. Atomically dispersed palladium driving reductive catalytic fractionation of lignocellulose into alkene-functionalized phenols. *ACS Catal.* **14**, 3565–3574 (2024).
26. Zhou, Y., Klinger, G. E., Hegg, E. L., Saffron, C. M. & Jackson, J. E. Multiple mechanisms mapped in aryl alkyl ether cleavage via aqueous electrocatalytic hydrogenation over skeletal nickel. *J. Am. Chem. Soc.* **142**, 4037–4050 (2020).
27. Prabhu, P. & Lee, J.-M. Influencing electrocatalytic processes through topographically disordered atomic sites. *Chem Catal.* **3**, 100621 (2023).
28. Baghestani, G., King, H. J. & Hocking, R. K. The functional role of disordered metal oxides from active catalysis to biological metabolism. *Adv. Energy Mater.* **14**, 2400281 (2024).
29. Liang, H.-W. et al. Molecular metal–N_x centres in porous carbon for electrocatalytic hydrogen evolution. *Nat. Commun.* **6**, 7992 (2015).
30. Li, J. et al. Combinatorial screening of Pd-based quaternary electrocatalysts for oxygen reduction reaction in alkaline media. *J. Mater. Chem. A* **5**, 67–72 (2017).
31. Sekol, R. C. et al. Pd–Ni–Cu–P metallic glass nanowires for methanol and ethanol oxidation in alkaline media. *Int. J. Hydrog. Energy* **38**, 11248–11255 (2013).
32. Szalaty, T. J., Klapiszewski, Ł. & Jesionowski, T. Recent developments in modification of lignin using ionic liquids for the fabrication of advanced materials—A review. *J. Mol. Liq.* **301**, 112417 (2020).
33. Prado, R. et al. Lignin oxidation and depolymerisation in ionic liquids. *Green Chem.* **18**, 834–841 (2016).
34. Cruz, M. G. A. et al. On the product selectivity in the electrochemical reductive cleavage of 2-phenoxyacetophenone, a lignin model compound. *Green Chem. Lett. Rev.* **15**, 153–161 (2022).
35. Di Marino, D., Stöckmann, D., Kriescher, S., Stiefel, S. & Wessling, M. Electrochemical depolymerisation of lignin in a deep eutectic solvent. *Green Chem.* **18**, 6021–6028 (2016).
36. Hart, W. E. S., Harper, J. B. & Aldous, L. The effect of changing the components of an ionic liquid upon the solubility of lignin. *Green Chem.* **17**, 214–218 (2015).
37. Singh, S. K. Ionic liquids and lignin interaction: An overview. *Bioresour. Technol. Rep.* **17**, 100958 (2022).
38. Liu, G. et al. Ionic liquid-trimetallic electrocatalytic system for C–O bond cleavage in lignin model compounds and lignin under ambient conditions. *Nano Res.* **17**, 2420–2428 (2024).
39. Liu, G. et al. Insights into the electrochemical degradation of phenolic lignin model compounds in a protic ionic liquid–water system. *Green Chem.* **23**, 1665–1677 (2021).
40. Ma, W. et al. Ionic liquids enhance the electrocatalysis of lignin model compounds towards generating valuable aromatic molecules. *J. Mol. Liq.* **367**, 120407 (2022).
41. Liu, G. et al. Electrocatalytic cleavage of C–C bonds in lignin models using nonmetallic catalysts at ambient conditions. *Chem Bio Eng.* **17**, 357–365 (2024).
42. Zhou, Y. et al. Electrocatalytic upgrading of lignin-derived bio-oil based on surface-engineered PtNiB nanostructure. *Adv. Funct. Mater.* **29**, 1807651 (2019).
43. Sahu, A., Rani, P., Subramaniam, A. & Pala, R. G. Even partially amorphous Pd₂Ni₂P metallic glass significantly promotes hydrogen evolution electrocatalysis. *Int. J. Hydrog. Energy* **47**, 23540–23551 (2022).
44. Chen, Y. et al. In-situ doping-induced crystal form transition of amorphous Pd–P catalyst for robust electrocatalytic hydrodechlorination. *Appl. Catal., B* **284**, 119713 (2021).
45. Yang, C., Magallanes, G., Maldonado, S. & Stephenson, C. R. J. Electro-reductive fragmentation of oxidized lignin models. *J. Org. Chem.* **86**, 15927–15934 (2021).
46. Wang, M. et al. Carbon modification of nickel catalyst for depolymerization of oxidized lignin to aromatics. *ACS Catal.* **8**, 1614–1620 (2018).
47. Luo, N. et al. Photocatalytic oxidation–hydrogenolysis of lignin β-O-4 models via a dual light wavelength switching strategy. *ACS Catal.* **6**, 7716–7721 (2016).

48. Ma, L., Zhou, H., Kong, X., Li, Z. & Duan, H. An electrocatalytic strategy for C–C bond cleavage in lignin model compounds and lignin under ambient conditions. *ACS Sustain. Chem. Eng.* **9**, 1932–1940 (2021).
49. Yu, K. et al. Ionic liquids screening for lignin dissolution: COSMO-RS simulations and experimental characterization. *J. Mol. Liq.* **348**, 118007 (2022).
50. Bulut, S. et al. Efficient cleavage of aryl ether C–O linkages by Rh–Ni and Ru–Ni nanoscale catalysts operating in water. *Chem. Sci.* **9**, 5530–5535 (2018).
51. Xie, J.-X. et al. Catalytic hydrolysis/hydrogenolysis of lignin-derived aryl ethers over bimetallic Pd–Ni systems: The directional regulation of reaction pathways. *ACS Sustain. Chem. Eng.* **11**, 12724–12738 (2023).
52. Mauriello, F., Paone, E., Pietropaolo, R., Balu, A. M. & Luque, R. Catalytic transfer hydrogenolysis of lignin-derived aromatic ethers promoted by bimetallic Pd/Ni systems. *ACS Sustain. Chem. Eng.* **6**, 9269–9276 (2018).
53. Lancefield, C. S., Ojo, O. S., Tran, F. & Westwood, N. J. Isolation of functionalized phenolic monomers through selective oxidation and C–O bond cleavage of the β -O-4 linkages in lignin. *Angew. Chem. Int. Ed.* **54**, 258–262 (2015).
54. Cao, B., Yang, H. & Yu, Z. A novel strategy for the characterization of self-assembled structures using the static solid-state phosphorus nuclear magnetic resonance technique. *J. Phys. Chem. Lett.* **15**, 262–266 (2024).
55. Li, Z., Wu, Z., Mo, G., Xing, X. & Liu, P. A small-angle X-ray scattering station at Beijing synchrotron radiation facility. *Instrum. Sci. Technol.* **42**, 128–141 (2014).
56. Martínez, L., Andrade, R., Birgin, E. G. & Martínez, J. M. Packmol: A package for building initial configurations for molecular dynamics simulations. *J. Comput. Chem.* **30**, 2157–2164 (2009).
57. Jorgensen, W. L., Maxwell, D. S. & Tirado-Rives, J. Development and testing of the OPLS all-atom force field on conformational energetics and properties of organic liquids. *J. Am. Chem. Soc.* **118**, 11225–11236 (1996).
58. Mark, P. & Nilsson, L. Structure and dynamics of the TIP3P, SPC, and SPC/E water models at 298 K. *J. Phys. Chem. A* **105**, 9954–9960 (2001).
59. Zeng, J., Duan, L., Zhang, J. Z. & Mei, Y. A numerically stable restrained electrostatic potential charge fitting method. *J. Comput. Chem.* **34**, 847–853 (2013).
60. Lu, T. & Chen, F. Multiwfn: A multifunctional wavefunction analyzer. *J. Comput. Chem.* **33**, 580–592 (2012).
61. Plimpton, S. Fast parallel algorithms for short-range molecular dynamics. *J. Comput. Phys.* **117**, 1–19 (1995).
62. Frisch, M. J. et al. Gaussian 09, Revision D.01. Gaussian, Inc., Wallingford, CT (2013).
63. Grimme, S., Antony, J., Ehrlich, S. & Krieg, H. A consistent and accurate ab initio parametrization of density functional dispersion correction (DFT-D) for the 94 elements H–Pu. *J. Chem. Phys.* **132**, 154104 (2010).
64. Kresse, G. & Furthmüller, J. Efficient iterative schemes for ab initio total-energy calculations using a plane-wave basis set. *Phys. Rev. B* **54**, 11169–11186 (1996).
65. Blöchl, P. E. Projector augmented-wave method. *Phys. Rev. B* **50**, 17953–17979 (1994).
66. Kresse, G. & Furthmüller, J. Efficiency of ab-initio total energy calculations for metals and semiconductors using a plane-wave basis set. *Comput. Mater. Sci.* **6**, 15–50 (1996).
67. Perdew, J. P., Burke, K. & Ernzerhof, M. Generalized gradient approximation made simple. *Phys. Rev. Lett.* **77**, 3865–3868 (1996).
68. Henkelman, G., Arnaldsson, A. & Jónsson, H. A fast and robust algorithm for bader decomposition of charge density. *Comput. Mater. Sci.* **36**, 354–360 (2006).
69. Wang, V., Xu, N., Liu, J.-C., Tang, G. & Geng, W.-T. Vaspkit: A user-friendly interface facilitating high-throughput computing and analysis using vasp code. *Comput. Phys. Commun.* **267**, 108033 (2021).
70. Vennström, M., Höwing, J., Gustafsson, T. & Andersson, Y. The crystal structures of PdNi₂P and Pd₈Ni₃₁P₁₆. *J. Solid State Chem.* **177**, 1449–1455 (2004).

Acknowledgements

This work was supported by the National Natural Science Foundation of China (22425806, 22278396, 22421003, 22338007, 22378392), CAS Project for Young Scientists in Basic Research (YSBR-105), the Beijing Natural Science Foundation (2252025), the beamline 1W2A of the Beijing Synchrotron Radiation Facility, and the BL14W1 beamline of Shanghai Synchrotron Radiation Facility (SSRF). We thank Dr. Wenxing Chen (Beijing Institute of Technology) for the aid of XAFS analysis.

Author contributions

H.Y.He, W.H. Wang, and S. J. Zhang supervised the project and proposed the idea. Z.Q. Zhai and Y.M. Lu conceived, designed, and performed the experiments. L.F. Ouyang prepared the catalyst. B. B. Cao performed the synchrotron radiation experiment. J. F. Lu, W. L. Ding, and Y. L. Wang carried out the simulations. Q. Zhao and F. Huo designed the FTIR experiment, Z.Q. Zhai, Y.M. Lu, H. Y. He, W.H. Wang, and S. J. Zhang co-wrote the paper. All the authors contributed to the discussion and analysis of the results.

Competing interests

The authors declare no competing interests.

Additional information

Supplementary information The online version contains supplementary material available at <https://doi.org/10.1038/s41467-025-58556-1>.

Correspondence and requests for materials should be addressed to Weihua Wang, Suojiao Zhang or Hongyan He.

Peer review information *Nature Communications* thanks Haohong Duan, Zupeng Chen and Wei Zhao for their contribution to the peer review of this work. A peer review file is available.

Reprints and permissions information is available at <http://www.nature.com/reprints>

Publisher's note Springer Nature remains neutral with regard to jurisdictional claims in published maps and institutional affiliations.

Open Access This article is licensed under a Creative Commons Attribution-NonCommercial-NoDerivatives 4.0 International License, which permits any non-commercial use, sharing, distribution and reproduction in any medium or format, as long as you give appropriate credit to the original author(s) and the source, provide a link to the Creative Commons licence, and indicate if you modified the licensed material. You do not have permission under this licence to share adapted material derived from this article or parts of it. The images or other third party material in this article are included in the article's Creative Commons licence, unless indicated otherwise in a credit line to the material. If material is not included in the article's Creative Commons licence and your intended use is not permitted by statutory regulation or exceeds the permitted use, you will need to obtain permission directly from the copyright holder. To view a copy of this licence, visit <http://creativecommons.org/licenses/by-nc-nd/4.0/>.

© The Author(s) 2025